BIOCHEMISTRY

Functional role of respiratory supercomplexes in mice: SCAF1 relevance and segmentation of the Q_{pool}

Enrique Calvo[1]*, Sara Cogliati[1,2]*, Pablo Hernansanz-Agustín[1]*, Marta Loureiro-López[1]*†, Adela Guarás[1], Rafael A. Casuso[2], Fernando García-Marqués[1], Rebeca Acín-Pérez[1], Yolanda Martí-Mateos[1], JC. Silla-Castro[1], Marta Carro-Alvarellos[1], Jesús R. Huertas[2], Jesús Vázquez[1,3]‡, J. A. Enríquez[1,4]‡

Mitochondrial respiratory complexes assemble into supercomplexes (SC). Q-respirasome (III_2 + IV) requires the supercomplex assembly factor (SCAF1) protein. The role of this factor in the N-respirasome (I + III_2 + IV) and the physiological role of SCs are controversial. Here, we study C57BL/6J mice harboring nonfunctional SCAF1, the full knockout for SCAF1, or the wild-type version of the protein and found that exercise performance is SCAF1 dependent. By combining quantitative data–independent proteomics, 2D Blue native gel electrophoresis, and functional analysis of enriched respirasome fractions, we show that SCAF1 confers structural attachment between III_2 and IV within the N-respirasome, increases NADH-dependent respiration, and reduces reactive oxygen species (ROS). Furthermore, the expression of AOX in cells and mice confirms that CI-CIII superassembly segments the CoQ in two pools and modulates CI-NADH oxidative capacity.

INTRODUCTION

The mitochondrial cristae are the main site of biological energy conversion through the respiratory complexes I to V known as oxidative phosphorylation system (OXPHOS). Respiratory complexes form superstructures called supercomplexes (SCs), among which the ones containing CI, CIII, and CIV were named respirasomes (*1*), from now on NADH (reduced form of nicotinamide adenine dinucleotide)–respirasome or N-respirasome. They are present in mitochondria from very different sources (*2*, *3*), they are able to respire (*4*), specific factors for the formation of some SCs have been found (*5*), and the cryo–electron microscopy structures of the N-respirasome (I + III_2 + IV) and the SC I + III_2 have been obtained (*6*–*8*). However, the physiological role of SCs is still under strong debate. A line of thinking proposes that SCs have no functional role (*9*). Other authors indicate that SCs optimize electron flux to gain efficiency in energy generation while minimizing reactive oxygen species (ROS) production (*5*, *10*). We proposed the "Plasticity Model," where individual and superassembled complexes coexist in a regulated equilibrium within the inner mitochondrial membrane (*4*, *11*). Thus, SCs rearrange in response to a shift in the metabolic source of electrons (*12*), in the metabolic adaptation of specialized cells in vivo (*13*), or to adapt the cell to different nutrients and physiological conditions (*14*, *15*). For instance, under starvation, the preferential use of fatty acids reduces the levels of SCs containing CI, so that free III_2 is more accessible to electrons coming from $FADH_2$ (reduced form of flavine adeninine dinucleotide) (*5*).

The controversy was centered on the biological role of SCAF1 in N-respirasomes and the role of SCs in the functional segmentation of the CoQ (Coenzyme Q or Ubiquinone) pool. In mouse, SCAF1 is 113 amino acid long and has a high homology in its C terminus with one subunit of CIV, for which there are two isoforms (COX7A1-80 amino acid and COX7A2-83 amino acid). The amino-terminal portion of the protein has no homology with any known protein. SCAF1 is required to superassemble CIII and CIV by replacing COX7A2 in the structure of CIV and by binding CIII through its amino-terminal portion (*16*). All inbred mouse C57BL/6 substrains investigated to date (*17*) harbor a nonfunctional version of SCAF1 (named $SCAF1^{111}$) that, due to a microdeletion that eliminates two amino acids, is unable to interact with CIV (*16*). In the absence of functional SCAF1, the SC III_2 + IV, herein named Q-respirasome, and the majority of SCs containing CI, CIII, and CIV cannot be formed (*5*, *16*, *18*). However, in some instances, particularly in heart mitochondria from C57BL/6 mice, a comigration between CI, CIII, and CIV suggestive of the presence of N-respirasomes can be observed (*16*, *18*). Therefore, the role of SCAF1 in the formation of the Q-respirasome (III_2 + IV) is today generally accepted; however, its role in the formation of the N-respirasome (I + III_2 + IV) is still questioned (*16*, *18*, *19*). This led to the hypothesis that factors different from SCAF1 may be responsible for the formation of SC I + III_2 + IV (*19*, *20*).

In addition, we observed, confirming previous results (*21*), that superassembly partially segments CoQ in two pools, one predominantly dedicated to flavin adenine dinucleotide (FAD) dependent enzymes and another to the oxidation of NADH by complex I (*5*). These data were obtained using isolated mitochondria. Using submitochondrial particles, opposite conclusions were reported (*22*), calling the partial CoQ partitioning hypothesis into question.

In this work, we first investigate the consequences of the ablation of SCAF1 in the performance of mice under intense exercise demand. Second, by combining data-independent proteomics, two-dimensional Blue native gel electrophoresis (2D-BNGE)–based structural analysis and functional studies of BNGE-enriched respirasome fractions, we determine the role of SCAF1 in the regulation of the structure of respirasome and its bioenergetics performance. Third, through the expression of AOX (alternative oxidase) in several cell systems and animals, we evaluate the potential segmentation of the CoQ pool induced by the superassembly between CI and CIII.

[1]Centro Nacional de Investigaciones Cardiovasculares Carlos III. Madrid 28029, Spain. [2]Institute of Nutrition and Food Technology, Biomedical Research Centre, Department of Physiology, University of Granada. [3]CIBERCV, Madrid, Spain. [4]CIBERFES, Madrid, Spain.
*These authors contributed equally to this work.
†Present address: Department of Biochemistry and Molecular Biology, University of Southern Denmark, Campusvej 55, 5230 Odense M, Denmark.
‡Corresponding author. Email: jvazquez@cnic.es (J.V.); jaenriquez@cnic.es (J.A.E.)

RESULTS

The ablation of functional SCAF1 compromises exercise performance

One of the more recurrent arguments to challenge the proposal that SCAF1 and the superassembly between complexes III and IV are bioenergetically relevant is the belief that all C57BL/6 mice substrains, which harbor a nonfunctional SCAF1, lack an apparent phenotype. Since this belief has never been experimentally addressed, we first investigated it in detail. We compared the phenotype of C57BL/6 mice with full ablation of SCAF1 ($SCAF1^{-/-}$ or $SCAF1^{KO}$), with the nonfunctional version of SCAF1 ($SCAF1^{111/111}$), and with the wild-type and functional version of this gene in homozygosis ($SCAF1^{113/113}$). We first confirmed that $SCAF1^{113/113}$ liver and heart mitochondria express high levels of SCAF1 that are associated substantially with the Q-respirasome and SC: III_2 + IV (Fig. 1A). On the other hand, and as described earlier (*16*), $SCAF1^{111}$ was very unstable and could only be found in minor amounts, interacting with CIII either in the I + III_2 or in III_2 (Fig. 1A). In the full knockout mice, no SCAF1 could be detected (Fig. 1A). The availability of these mice with identical genome but harboring or not a functional SCAF1 protein allowed us to test for potential phenotypic differences. We thus evaluated the exercise performance of the different groups of animals under highly energetic demands. We found that $SCAF1^{113}$ mice were able to reach a 30% higher maximum speed in the treadmill than any other group of animals, regardless of the sex of the animals (Fig. 1B). These results demonstrate that the absence of $SCAF1^{113}$ affects the physiology of mice and that $SCAF1^{111}$ does not retain any relevant functionality.

The observation that SCAF1 ablation causes such evident phenotype suggests that SCAF1 may increase the efficiency of the electron transport chain by regulating SC formation. Hence, we took a deeper look into the molecular role of this protein in the function of the OXPHOS system, aiming to further solve the controversy on this issue. We first reevaluated the molecular evidence of the formation of complexes and SCs and the structural impact of SCAF1 by unbiased complexome analysis in a variety of tissues and cell lines. We then evaluated the interaction of respiratory complexes within SCs by 2D-BNGE analysis. Last, we performed a functional analysis of enriched fractions of complexes and SCs in the presence or in the absence of functional SCAF1.

The tissue-specific distribution respiratory complexes is due to superassembly

Mitochondria-enriched preparations from heart, brain, and liver from CD1 mice and from the cell line L929 repopulated with mitochondrial DNA (mtDNA) from C57BL/6mice ($L929^{C57}$), having all of them the wild-type functional version of SCAF1, were separated by BNGE, and each lane was cut into 26 slices; each slice was subjected to trypsin protein digestion and analyzed by mass spectrometry (MS) using the data-independent scanning (DiS) method we previously developed (*12*, *16*). We identified 1134 proteins classified as mitochondrial in the Mitocarta 2.0 (*23*), which correspond to 98% of all Mitocarta-annotated proteins (fig. S1A). Mitochondrial enrichment was different between samples, being heart (81% of peptide identifications annotated in Mitocarta) and liver (71%) more enriched in known mitochondrial proteins, while brain showed a lower enrichment (38%) (fig. S1B). In all cases, an almost complete coverage of components of OXPHOS complexes was achieved (data file S1). Every subunit from CII and CIII was identified (fig. S1C), together with 41 of the 44 annotated proteins from CI (fig. S1C).

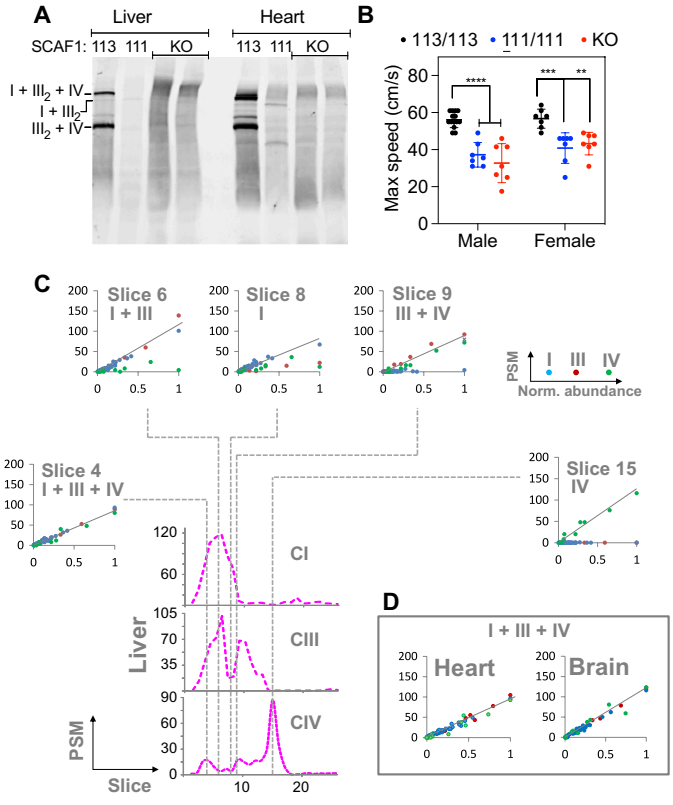

Fig. 1. SCAF1-deficient phenotype and Blue-Dis characterization of SCs. (**A**) BNGE followed by Western blot with anti-SCAF1 antibody showing the absence or presence of SCAF1 in the indicated tissue and mouse strain. 113: C57BL/6JOlaHsd mice with the functional version of SCAF1; 111: C57BL/6JOlaHsd mice (it harbors a nonfunctional version of SCAF1); KO: C57BL/6JOlaHsd mice without SCAF1. (**B**) Effect of SCAF1 on the maximum speed running in a treadmill by the indicated mouse groups. (**C**) Blue-DiS evidence of the formation of OXPHOS SCs. For each complex, the number of protein peptide-spectrum matches (PSMs) was plotted against normalized protein abundances (see Materials and Methods), showing that the relative proportions of proteins from CI (blue points), CIII (red points), and/or CIV (green points) are constant in specific BNGE slices from liver mitochondria indicating the presence of multimeric structures. Slices 2 to 4 correspond to a ternary structure (I + III + IV), slices 5 to 6 and 9 to 10 to binary structures (I + III and III + IV, respectively), and slices 8 and 15 to monomeric forms (I and IV, respectively). (**D**) Similar results are obtained in heart and brain mitochondria; for simplicity, only one slice with the tertiary structure is shown.

Concerning CIV, this complex is built of 14 proteins but several of them have isoforms making up a total of 21 possible components. However, COX6B2 and COX7B2 are both expressed only in sperm, and COX4i2 only in lung and carotid body, so that 18 proteins were potentially identifiable in our samples, from which we detected 16 (fig. S1C). Regarding CV, we could detect 17 of the 20 structural proteins of this complex (fig. S1C). Apparent molecular weights could be accurately assigned to each one of the 26 BNGE slices from the known masses of individual complexes and of SC (fig. S1D). The performance of the Blue-DiS technology, which significantly enhances coverage, reproducibility, and sensitivity with respect to regular complexome analysis (*12*, *16*), allowed us to perform a high-resolution quantitative mitochondrial complexome profiling from a completely hypothesis-free perspective.

Thus, it allowed cross-correlation analysis of protein abundances across different slices within the same mitochondrial type (fig. S2A). This analysis confirmed that the relative abundances of all proteins belonging to CI, CIII, CIV, or CV were constant across slices (fig. S2A and table S1). Moreover, the most representative slice from each complex also had the same protein proportions across the different mitochondrial types (fig. S2B and table S2), despite the fact that the electrophoretic mobility protein distributions profiles of CI, CIII, and CIV, but not of CV, were markedly different from one mitochondrial source to another (fig. S2, C and D). Thus, complexes in different tissues have the same protein composition but form tissue-specific high molecular weight structures.

Notably, the larger structures (slides 1 to 8) consistently contained identical proportions of CI and CIII or CIII and CIV proteins (Fig. 1, C and D). Cross-correlation analysis confirmed that the protein composition in the I + III + IV, I + III and III + IV structures was maintained between the adjacent slices (Fig. 2A) and between tissues (Fig. 2B), reflecting the formation of SC in an unbiased manner.

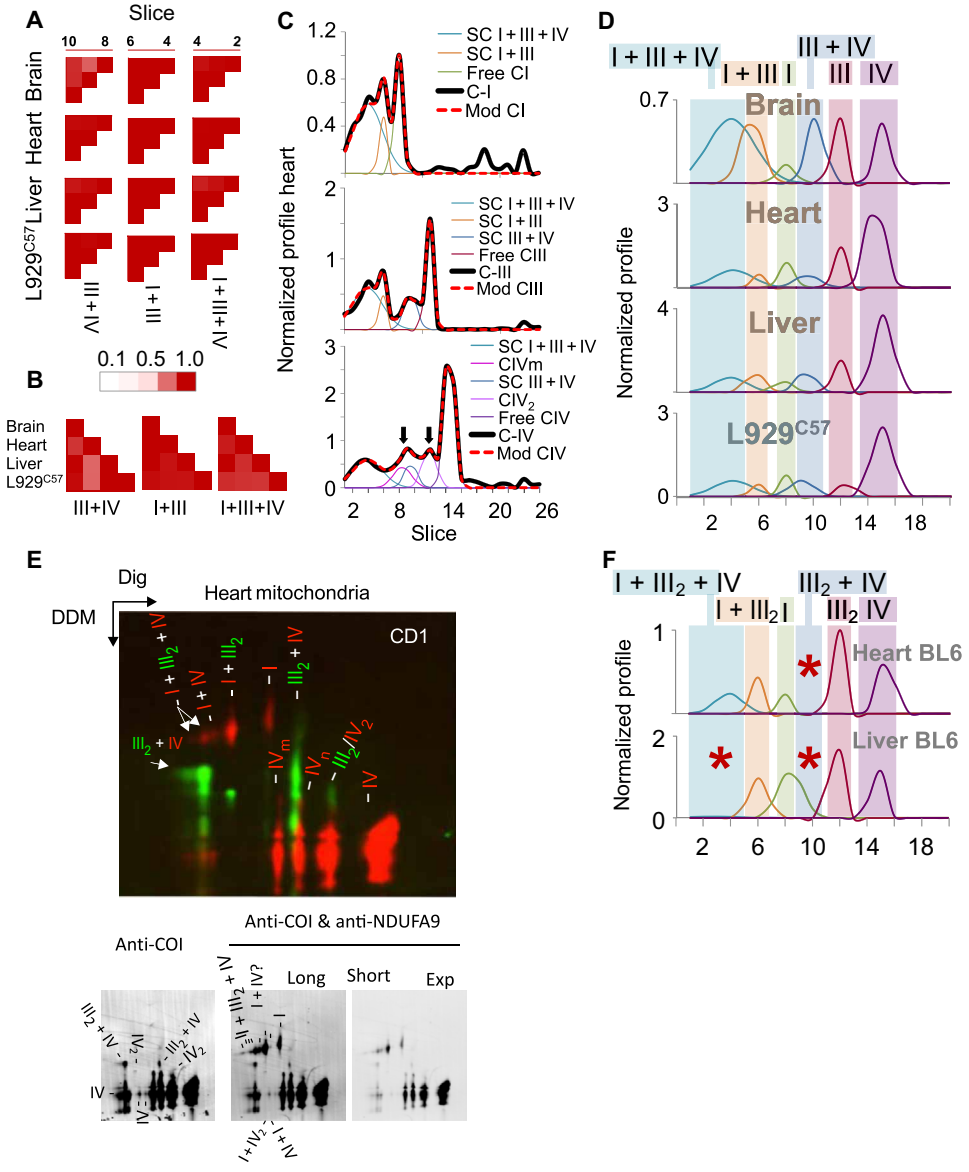

Fig. 2. Further characterization of SCs by Blue-DiS. (**A**) Cross-correlation analysis of SC protein abundances for the indicated slices. (**B**) Cross-correlation analysis of SC protein abundances for the indicated mitochondrial types. (**C**) Normalized profiles of CI, CIII, and CIV from heart mitochondria (black lines) are accurately explained as a superimposition (red dashed lines) of six Gaussian peaks corresponding to monomeric and multimeric structures. For CIV, two additional peaks (CIV_2 and CIV_m) had to be added to the model to explain the normalized profile (arrows). (**D**) Gaussian components modeling of the normalized profiles for the four mitochondrial types. (**E**) Top: 2D-BNGE (Dig/DDM) analysis of heart mitochondria resolving complexes and supercomplexes in the first dimension and disrupting SCs into their component complexes in the second dimension. NDUFA9 in red indicates the migration of CI, COI in red indicates migration of CIV, and CORE2 in green indicates migration of CIII. (E) Bottom: Split channels from the above panel. COI immunodetection was performed first to indicate migration of CIV-containing structures, and NDUFA9 immunodetection indicates migration of CI containing structures. This gel corresponds to that shown in Fig. 5E where the immunodetection of CORE2 to localize CIII is also included. (**F**) Gaussian deconvolution of the heart- and liver-normalized profiles from BL6 mice, with an impaired SCAF1 protein. Asterisks indicate the position of SC III2 + IV (completely absent in both tissues) and of the respirasome, which is absent in the liver but remains detectable in the heart.

While qualitative evidence about the formation of SCs is broadly known, a reliable quantitative estimation of the distribution of these structures in different tissues is lacking. Hence, we modeled the complete migration profiles of CI, CIII, and CIV by unsupervised Gaussian deconvolution. We found that in all mitochondrial types, the profile of CI and CIII could be accurately explained as a superimposition of broad Gaussian peaks corresponding to a ternary complex (I + III + IV), to binary I + III and III + IV structures, and to free CI, CIII, and CIV forms (red dashed lines in Fig. 2C and fig. S2D), having these components the same electrophoretic mobilities and similar peak widths across all mitochondrial sources (Fig. 2D). We also found that the profile of CIV could not be adequately explained by these structures around slices 6 to 12 (Fig. 2C, black arrows), suggesting the presence of significant amounts of CIV dimers and multimers. Thus, the addition of two more CIV structures (IV_2 and IV_m) was sufficient to model the migration profile of this complex in all mitochondrial types (red dashed lines in Fig. 2C and fig. S2D).

Since comigration in BNGE is necessary but insufficient to demonstrate interaction, we performed a Blue-DiS analysis of mitochondria from cultured mutant cell lines that are unable to assemble one or more of the complexes (*24*–*26*). As expected, the cell line ΔCI, which lacks the ND4 subunit from CI and is unable to assemble CI (*26*), neither free CI nor SCs I + III_2 and I + III_2 + IV, could be detected (fig. S3, A and B); however, free III_2 and IV and the SC III_2 + IV were detected at the expected sizes (green rectangles in fig. S3, A and B). In the case of the mutant cell line for Cox10 protein (ΔCIV), which lacks assembled CIV, all structures containing CIV were absent (red rectangles in fig. S3, A and B). In addition, the structures containing CI could neither be detected, in agreement with the fact that CIV is needed for the stabilization of CI (*24*); hence, in this mutant, only the free III_2 form was detectable (green rectangles in fig. S3, A and B). Last, in the Rho 0 cell line, which lacks mtDNA encoding for different subunits of the respiratory complexes, none of these structures were observed (red rectangles in fig. S3A). However, CII, which is totally encoded in the nucleus, and a CV form of smaller size (V*) remained detectable in these cells (fig. S3A).

In summary, using unbiased techniques with increased coverage and quantitative accuracy, we confirm that the complete size distributions of OXPHOS components in a variety of mitochondrial types can be explained by a set of structures of the same size and protein composition that are present at different relative proportions (Fig. 2D).

Blue-DiS complexome analysis allows determining the stoichiometry of the N-respirasome

As several bands appear in the upper part of Blue native gels, it has been generally assumed that there are multiple types of N-respirasomes with a stoichiometry of 1:2 between CI and CIII, which differed in their increasing content of 1 to 4 CIV monomers. This derives from an early work by Schägger and Pfeiffer (*27*) in which the precise stoichiometry of 1:2 between CI and CIII in the respirasome was measured while that of CIV was only tentatively proposed, as it could not be confirmed experimentally. This caution was explicitly highlighted by the authors; however, many reports accepted the proposed stoichiometry as a proven fact.

We took advantage of the good linear response of quantitative Blue-DiS protein values (Fig. 1, C and D, and fig. S2A) to estimate the relative molar stoichiometries of complexes within each slice (fig. S3, C and D, see Materials and Methods for detailed explanation). From slices 2 to 6, the relative molar proportion CIII:CI was 2:1, in the four mitochondrial types, implying that the proportion I + III_2 is constant in the respirasome and in the SC formed by CI and CIII (fig. S3E). This is in full agreement with the stoichiometry determined by Schägger. Besides, the relative molar proportions CI:CIV and CIII:CIV were 1:1 and 2:1, respectively, between slices 2 and 4, implying that the respirasome has an exclusive composition of I + III_2 + IV (fig. S3E).

To our knowledge, these are the first stoichiometry estimations of OXPHOS complexes made by mass spectrometry, which agree with the structures analyzed by cryo–electron microscopy (*6*–*8*), and contradict the experimentally unsupported but generalized tendency to assume that there are multiple types of respirasomes that differed in their increasing content of 1 to 4 CIV monomers. The reason for the split of the respirasome in several discrete bands in BNGE, corresponding to a broad peak in Blue-DiS analysis, remains to be elucidated. In slices 5 and 6, CIV is still detected although at a lower proportion, suggesting that in this area migrates CIV superstructures of unknown composition (fig. S3E). Slices 7 and 8 are enriched in CI, where it migrates as a free complex, but again with the significant presence of CIV in different high molecular weight structures. Last, the relative proportions of CIII and CIV in bands 9 and 10 are coherent with a stoichiometry 2:1 (SC: III_2 + IV) (fig. S3E). In summary, unbiased Blue-DiS analysis reinforces the results obtained by other techniques and provides complementary evidence that OXPHOS complexes are arranged into SC at fixed stoichiometries.

CIV forms previously unidentified SCs

Our complexome analysis predicts that several structures that contain CIV, not yet molecularly characterized, should be present. These are not only CIV structures above and below the Q-respirasome (III_2 + IV) but also some CIV structures of higher molecular weight migration around SC I + III_2 and SC I + III_2 + IV. The existence IV_2 is well documented, and high molecular weight entities containing only CIV have been described elsewhere (*16*). To confirm whether the CIV structures predicted by Blue-DiS analysis are true entities, we performed 2D-BNGE of CD1 heart mitochondria using in the first-dimension digitonin as detergent to preserve the integrity of SCs and *n*-dodecyl-β-D-maltoside (DDM) in the second dimension to disaggregate SCs into their component complexes. This procedure partially preserves the interaction between CIII and CIV and the IV_2 (*25*). As shown in Fig. 2E, this analysis confirmed the presence of IV_2 and two forms of CIV that migrate immediately faster and slower than SC III_2 + IV and that do not superassemble with any other respiratory complex (IVm and IVn in Fig. 2E). These three structures account for a significant proportion of the CIV in heart samples. In addition, we detected the presence of low proportions of a putative SC: I + IV_2, which migrates with SC I + III_2 and segregates into CI and dimer CIV (Fig. 2E), and of a putative SC I + IV, which migrates between free CI and SC: I + III_2 (Fig. 2E).

More unexpectedly, we found CI and CIV monomer, but without CIII, migrating together between SC: I + III_2 + IV and SC I + III_2, very close to the lowest-migrating N-respirasome (I + III_2 + IV) band (Fig. 2E, labeled as I + IV). The reason why this putative SC migrates with the apparent molecular weight of a respirasome is unclear and may indicate that this structure interacts with a yet to discover mitochondrial inner membrane component. Therefore, 2D-BNGE analysis of heart mitochondria reveals specific SCs that contain CIV, confirming Blue-DiS predictions, and also new interactions between CIV and CI which will deserve further investigation. Note that, because

of their relatively low abundances, these additional IV structures are fully compatible with both the Gaussian models of CI and CIV and the stoichiometries determined from Blue-DiS profiles.

SCAF1 is the only detectable protein significantly associated with N- and Q-respirasomes

The role of SCAF1 in the formation of the Q-respirasome (III_2 + IV) is today generally accepted; however, its role in the formation of the N-respirasome (I + III_2 + IV) is still questioned, mainly due to the fact that comigration of CI, CIII, and CIV can still be observed in the absence of functional SCAF1 (*16*, *19*). This led to the hypothesis that factors other than SCAF1 may be responsible for the formation of SC I + III_2 + IV (*19*, *20*). To clarify this point, we took advantage of the high-resolution and sensitivity that allows the Blue-DiS complexome analysis to search for potential interaction partners of specific SC structures. We generated their reference migration profiles in silico by combining the SC profiles obtained by deconvolution analysis and performing a correlation search for all identified proteins displaying a similar profile. As expected, this analysis led to a natural, hypothesis-free detection of Cox7a2l/SCAF1 with a significant correlation in all the mitochondrial types with the structures containing CIII and CIV together, including the N-respirasome [fig. S4A (left) and B]. Consistently, deletion of CI inhibited the migration of SCAF1 in the position of the respirasome, but not in the position of SC III_2 + IV, and no traces of SCAF1 were detected in the mutant lacking CIV or in Rho 0 cells (fig. S4A, right). The correlation analysis did not detect any further candidate protein showing significant correlation with SCs. In summary, we provide further experimental evidence that SCAF1 is the only detectable protein specifically associated with both the N- and the Q-respirasomes, supporting the findings we presented in previous reports (*5*, *16*).

SCAF1 confers structural attachment between III_2 and IV within the N-respirasome

To explore the structural impact of the presence of SCAF1, we analyzed by Gaussian deconvolution the Blue-DiS profiles of mitochondria prepared from C57BL/6JOlaHsd SCAFI^{111} heart and liver mitochondria. As shown in Fig. 2F, in BL6 liver, the peaks corresponding to the respirasome and the SCs III_2 + IV disappeared (red asterisks), while the rest of structures, including SCs I + III_2 and the III_2 peaks, were maintained. However, while SC III_2 + IV was neither observed in BL6 heart, the presence of the respirasome remained clearly detectable in this tissue (Fig. 2F), reconfirming our previous observations (*16*).

We reasoned that if the role of SCAF1 is to physically link CIII and CIV, and this function is maintained in the respirasome, then mitochondria harboring SCAF1^{113} and SCAF1^{111} should have different types of respirasomes differing structurally in the interaction between CIII and CIV. To experimentally evaluate this hypothesis, we took advantage of the fact that upon 2D-BNGE analysis, the second dimension used to disaggregate SCs (which uses DDM) does retain significant amounts of the III_2 + IV association, allowing us to discern whether CIII and CIV are physically linked or not in the respirasome in the absence of functional SCAF1. We performed 2D-BNGE with liver mitochondria derived from CD1, C57BL/6JOlaHsd mice, and also from C57BL/6JOlaHsd harboring the wild type version of SCAF1 (SCAF1^{113}) generated in our laboratory (*16*). This approach confirmed again that heart mitochondria from BL6 mice do not assemble SC III_2 + IV (Fig. 3, A and B) and clearly demonstrated that the III_2 + IV structure remains within the respirasomes

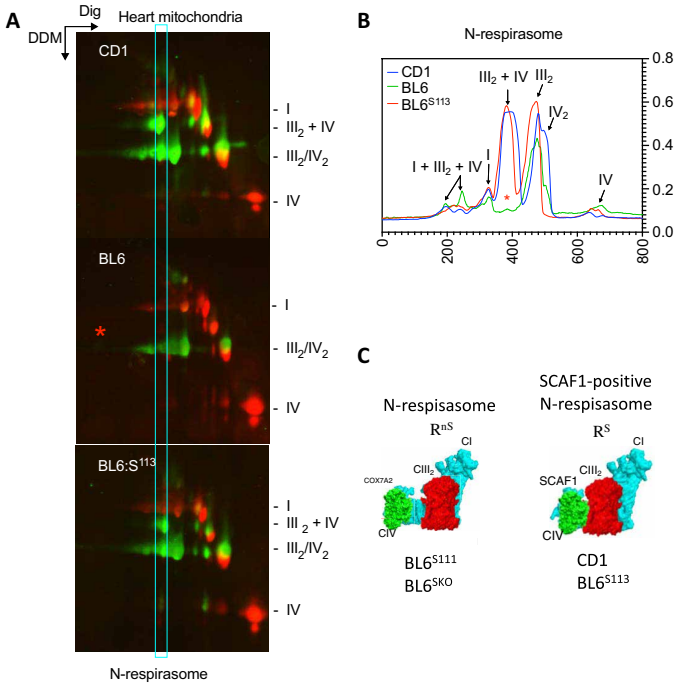

Fig. 3. Structural consequences of SCAF1 deficiency in the formation of SCs. (**A**) 2D-BNGE (Dig/DDM) analysis of heart mitochondria resolving complexes and SCs in the first dimension and disrupting SCs into their component complexes in the second dimension. NDUFA9 immunodetection in red indicates the migration of CI, COI immunodetection in red indicates migration of CIV, and CORE2 immunodetection in green indicates migration of CIII. Samples from BL6, CD1, and BL6:S^{113} heart are compared highlighting the area of migration of the N-respirasome. Red asterisk indicates the absence of the respirasome-derived III_2 + IV only in the BL6 sample, indicating that III_2 + IV is not physically linked to SCAF1-deficient respirasomes (**B**) Different traces corresponding to the N-respirasome area of (A). (**C**) Representation of the two structurally different respirasomes. RS, SCAF1-postive N-respirasome; RnS, SCAF1-negative N-respirasome.

containing functional SCAF1 (CD1 and SCAF1^{113}) but not in those with the nonfunctional form (BL6 with SCAF1^{111}) (Fig. 3, A and B). In conclusion, this analysis demonstrates that SCAF1^{+} and SCAF1^{-} respirasomes are structurally different (Fig. 3C).

SCAF1 enhances respiratory performance and reduce ROS production by the N-respirasome

We then inquired whether the structural difference linked to the presence of an active SCAF1 form in the respirasome has any impact on their respiratory capacity. We first evaluated the suitability to perform kinetic analyses by studying isolated individual complexes (I, III_2, and IV) and the feasibility to measure the rate of oxidation/reduction of their respective electron donors/acceptors, considering their expected stoichiometries. All the rates of the individual complexes were similar regardless the strain of origin, with the exception of a mild reduction in CIII activity in BL6^{113} (fig. S4, C to E). Next, we excised BNGE bands containing SC I + III_2 + IV (respirasome) from SCAF1^{113} (CD1, BL6^{113}, and 129 mice) and SCAF1^{111} (C57BL/6J mice) heart mitochondria and determined their respiratory capacity using NADH as substrate in a Clark electrode (*4*) and their NADH oxidation capacity by spectrophotometry (Fig. 4A). For normalization purposes, we determined the respiration capacity induced by TMPD (*N*,*N*,*N*′,*N*′-Tetramethyl-*p*-phenylenediamine) in the same samples after inhibition with antimycin and rotenone; we also

normalized by the protein content determined after eluting the respirasome from the gel. We found that both N-respirasomes, regardless if it contains SCAF1, were able to perform NADH-dependent respiration without the need of adding either external CoQ or cytochrome c (Cyt c) (Fig. 4B). The respiratory capacity of the N-respirasome was much lower than that of CIV monomer, and NADH oxidation was also decreased in comparison to that of CI. These results suggest, in agreement with a recent observation on amphipol-stabilized SC:I + III_2, that superassembly of respiratory complexes modulates their activity (*28*). Moreover, the rate of respiration by SCAF1 containing N-respirasomes from different sources was about one order of magnitude higher than that of those lacking SCAF1, regardless of whether they are normalized by CIV-dependent respiration (Fig. 4C) or by protein content (Fig. 4D). In agreement with this observation, the rate of NADH oxidization by $SCAF1^+$ respirasomes was between three and four times higher (Fig. 4E).

Lenaz's laboratory showed by reconstruction in liposomes that the association between CI and CIII into SCs reduces the production of

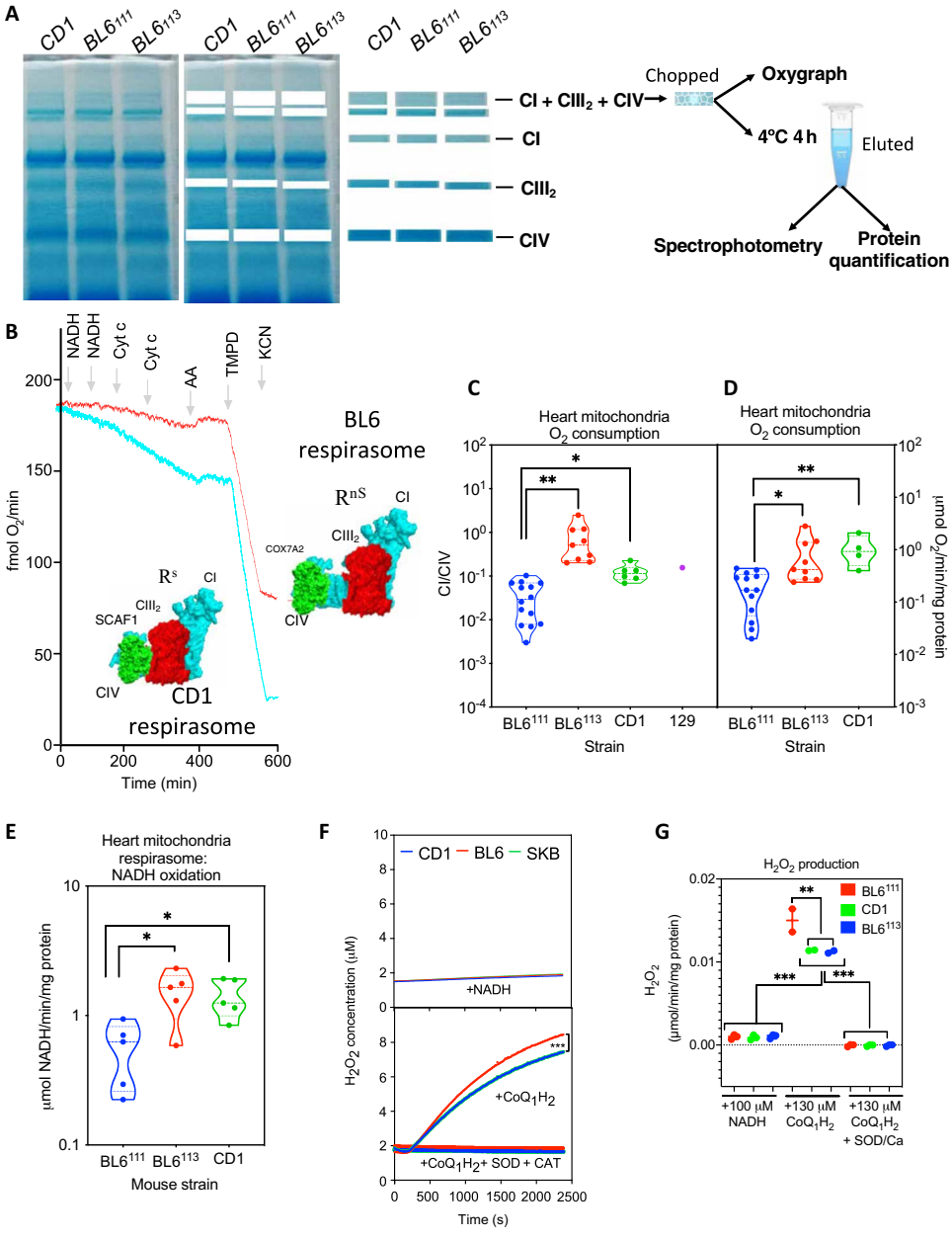

Fig. 4. Functional consequences of SCAF1 deficiency in the activity of the N-respirasome. (**A**) Scheme representing the experimental setup to analyze the function of the respirasomes. (**B**) Representative oxygen consumption traces obtained with heart respirasomes excised from the BNGE and derived from either C57BL/6 or CD1 animals. The addition of different components is indicated. (**C** and **D**) NADH-dependent respiration rate normalized by TMPD respiration rate (C) or by milligram of protein (D) of heart respirasomes excised from BNGE from the indicated mouse strain and measured in a Clark oxygen electrode. (**E**) NADH oxidation rate by heart respirasomes eluted from BNGE excised bands of the indicated mouse strain and measured by spectrophotometry. (**F** and **G**) Representative traces (F) and quantitative data (G) of H_2O_2 production upon NADH oxidation (top) or $CoQH_2$ oxidation (bottom) by heart respirasomes eluted from BNGE excised bands of the indicated mouse strain and estimated by Amplex Red. When $CoQH_2$ oxidation was assayed, rotenone was included to prevent the interaction of $CoQH_2$ with CI, and the assay was performed. *P < 0.05; **P < 0.01; ***P < 0.001.

ROS (*10*). This observation was validated in vivo by others (*14*, *29*). The availability of respirasomes with different degrees of interaction between III_2 and IV allowed us to investigate whether this interaction also affects on the production of ROS. For this purpose, we incubated the BNGE-excised respirasome bands from CD1, $BL6^{111}$, and $BL6^{113}$ heart mitochondria preparations in the presence of NADH and Amplex Red to monitor ROS production. We found no differences in the level of ROS produced by the respirasomes from any of the investigated strains (Fig. 4, F and G). Considering that the rate of respiration and NADH oxidation of $SCAF1^-$ N-respirasome is lower than its $SCAF1^+$ counterpart, we calculated that the N-respirasome lacking SCAF1 derived 0.185% of NADH electrons to ROS, whereas that with SCAF1, from either CD1 or $BL6^{113}$ derived 0.064 and 0.067%, respectively. Next, we repeated the experiment but substituting NADH by CoQ_1H_2 to donate electrons to CIII and in the presence of rotenone to block CI interaction with CoQ. Under these conditions, which mimic a stress situation with an abnormal rise in $CoQH_2$, $SCAF1^-$ respirasomes produced significantly more ROS (Fig. 4, F and G). In all cases, ROS production was fully quenchable by the addition of superoxide dismutase and catalase (Fig. 4, F and G). Therefore, $SCAF1^+$ respirasomes produced less ROS than $SCAF1^-$ ones. In summary, although SCAF1 can be dispensable for the formation of respirasomes, it confers structural attachment between complexes III_2 and IV within the respirasomes providing more stability, significantly better functional performance and lower production of ROS.

Proteolytic processing of SCAF1 induces the transition between tight and loose N-respirasomes

The existence of two structurally distinct respirasomes was described recently in ovine (*6*) and confirmed later in bovine models (*8*). One form of respirasome has complexes III_2 and IV tightly attached (named tight respirasome), while the other is characterized by an increased distance between them (named loose respirasome). Our observation that SCAF1 determines the interaction between III_2 and IV within the N-respirasome is reminiscent of the existence of tight and loose respirasomes. Noticeably, both ovine and bovine SCAF1 sequences match the mouse wild-type and functional 113 version.

Letts and co-workers observed that the proportion between both respirasome forms in a given preparation is not stable. After overnight incubation at 4°C, the tight respirasomes were transformed into the loose ones (*6*). We wondered whether this phenomenon could be observed by BNGE analysis. Thus, we compared CD1-liver mitochondria (which harbors functional SCAF1), maintained several hours in the refrigerator, before and after solubilization with digitonin. Unexpectedly, both SCs I + III_2 + IV and III_2 + IV, but not SC I + III_2, disappeared in the samples maintained at 4°C only if they were previously digitonized (Fig. 5A). In addition, SCAF1 migrated as a bulk with the free CIV in the digitonized preparations (Fig. 5, A and B). Furthermore, 2D-BNGE/SDS–polyacrylamide gel electrophoresis (PAGE) analysis revealed that the form of SCAF1 that migrated with free CIV (marked with an asterisk) had a smaller molecular weight than the canonical form (Fig. 5C). Proteomic analysis demonstrated that in slices corresponding to SC I + III_2 + IV, IV_2, and IV, a peptide spanning the sequence SSVTAYDYSGK (originated from the corresponding SCAF1-derived tryptic peptide LTSSVTAYDYSGK) was unequivocally identified, exclusively in the nonfresh samples (Fig. 5E and fig. S5A). This sequence was mapped into the N-terminal region of the protein, which contains the CIII-interacting domain (*16*) (underlined sequence in Fig. 5D). Further

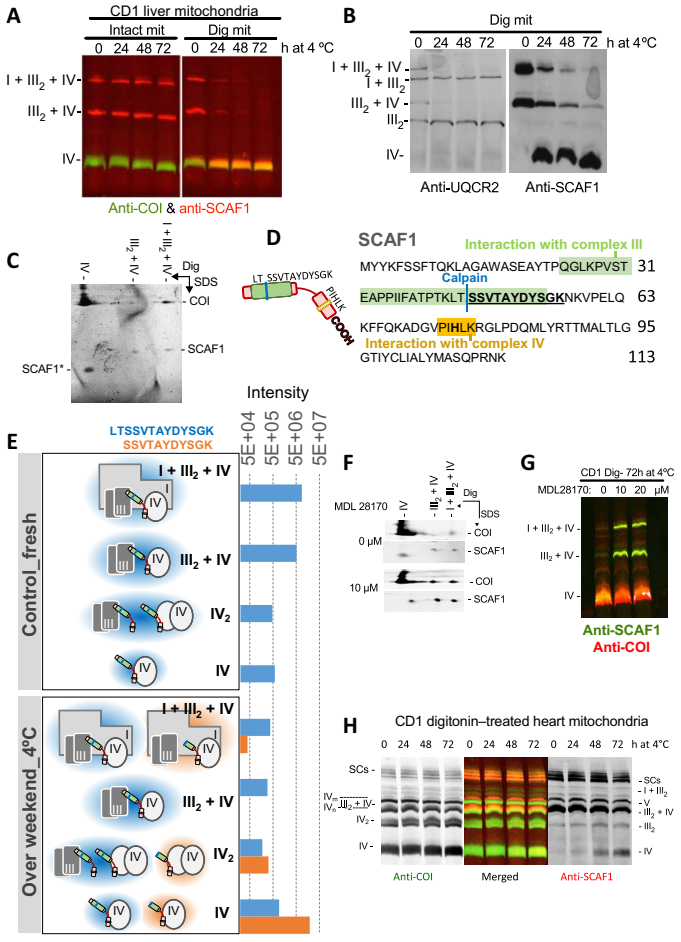

Fig. 5. SCs are unstable upon mitochondrial membrane disruption. (**A**) BNGE resolving complexes and SCs from CD1 liver from intact or digitonized mitochondria preincubated during the indicated time at 4°C and probed with the indicated antibody. (**B**) BNGE resolving complexes and SCs from CD1 liver from digitonized mitochondria preincubated during the indicated time at 4°C and probed with the indicated antibody. (**C**) 2D-BNGE/PAGE resolving complexes and SCs in the first dimension and protein components in the second dimension from CD1 liver digitonized preparation preincubated 72 hours at 4°C, showing that SCAF1 is processed (SCAF1*). The membrane was immunoblotted with the indicated antibodies. (**D**) Structure of SCAF1 sequence, mapping CIII-interacting regions (in green) and CIV-interacting regions (in yellow). The predicted calpain-1 processing site is indicated with a blue line. (**E**) Quantitative analysis of the SCAF1-derived tryptic (LTSSVTAYDYSGK, in blue) and calpain-1–processed (SSVTAYDYSGK, in orange) peptides. Both peptides were quantified in the BNGE slices corresponding to SCs I + III_2 + IV and III_2 + IV and to IV_2 and to CIV in fresh or in 4°C-incubated liver mitochondria-enriched fractions. The calpain-1–processed peptide was only detected in the nonfresh preparations, attached to CIV and IV_2 and also to the respirasome. A structural interpretation of these results is presented at the left; the blue and orange shadows indicate whether the SCAF1 peptide is tryptic or processed, respectively. (**F**) 2D-BNGE/PAGE showing that the proteolytic cleavage of SCAF1 can be prevented by inhibition of calpain-1. (**G**) BNGE/PAGE analysis of liver mitochondria showing that the stability of the respirasome and the SC III2 + IV is preserved after digitonization in the presence of a calpain-1 inhibitor. (**H**) BNGE profile for CIV (COI, red) and SCAF1 (green) in heart samples maintained at 4°C after digitonization during the indicated times.

quantitative analysis revealed the coexistence of the intact and proteolyzed forms of the peptide bound to CIV in the respirasome, while SC: III_2 + IV contained only the intact form (Fig. 5E). These results indicate that SCAF1 suffers a partial proteolytic processing

that disrupts SC: III_2 + IV, destabilizes the respirasome, and parallels the loss of CIV-containing SCs. In silico analysis of the processing site in SCAF1 revealed a putative cleavage site for calpain-1 (Fig. 5D). In agreement with this prediction, the use of calpain inhibitors was sufficient to prevent the cleavage of SCAF1 (Fig. 5F) and also to preserve the integrity of CIV-containing SC after digitonin treatment (Fig. 5G). When similar experiments were repeated with mitochondrial samples purified from CD1 heart, we also observed the relocation of SCAF1 with free CIV, but the reduction in the amount of CIV-containing SC was, although evident, much milder (Fig. 5H). All these results indicate that SCs are unstable and can shift from tight (e.g., kinetically active) to loose (e.g., kinetically restrained) forms when mitochondrial membrane integrity is compromised, likely as a consequence of the release of calpain-1.

We wondered whether other proteases and/or lipases could be released upon mitochondrial disruption that could gain access to the inner mitochondrial membrane and disrupt the respiratory complexes or SCs. To further study this issue, we subjected digitonized and intact mitochondria from liver (fig. S5B) and heart (fig. S5C) preparations to prolonged incubations at different temperatures. Digitonized liver mitochondria completely lost the N- and Q-respirasomes after 72 hours at 4°C and all SCs, including SC I + III_2, after 3 hours at 37°C (Fig. 5A and fig. S5B). Respirasomes from digitonized heart mitochondria were more stable than those from liver at 4°C (72 hours) but were completely lost after 3 hours at 37°C; at this temperature, also the CIV monomer disappeared (fig. S5C). In contrast, all of these structures remained stable in intact organelles (fig. S5, B and C). More worrying is the fact that the stability of both heart and liver SCs is not maintained if digitonized mitochondria are incubated at 37°C for just 1 hour (fig. S5D). All these observations call to caution when performing experiments in disrupted mitochondria.

Our unexpected results prompted us to evaluate whether BNGE purified respirasomes were stable enough during functional studies to trust the conclusions presented above. To address this issue, we kept the first-dimension gel for 1 or 3 hours at 37°C after running the BNGE to inquire whether the respirasomes are preserved. After the incubation period, we ran a second-dimension electrophoresis also in the presence of digitonin to determine the intactness of structures, since complexes and SCs are expected to migrate forming a diagonal unless some associations are disrupted during incubation. After 1- or 3-hour incubation at 37°C, the respirasome and any other detected complex or SCs remained substantially intact apart from comet tail–like shape of the spots due to diffusion in the first-dimension gel during the long period of incubation (fig. S5E). Moreover, 2D-BNGE analysis, using DDM in the second dimension to dissociate the respirasomes, confirmed the stability of the interaction between III_2 and IV within the respirasome (fig. S5F). Therefore, BNGE allows the isolation of the respirasome maintaining its structure intact to perform functional studies, validating our functional observations.

Superassembly between CI and CIII partially segments the CoQ pool

One of the more controversial issues regarding respiratory SCs is the proposal of substrate channeling between CI and CIII. Evidences in favor of this proposal were provided by flux control analysis (*21*) and by experiments in cell lines in which all available CIII was superassembled with CI (*5*). These evidences were questioned by either discrepant flux control experiments (*30*) or by experiments where recombinant AOX was added to a preparation of submitochondrial particles (*22*). The latter infers that the interaction of CI and CIII in SCs does not modify the delivery of electrons to the alternative oxidase AOX by CoQ. These results led to the conclusion that there is a unique CoQ pool equally accessible to CI and CII within mitochondrial inner membrane.

Given the observation that the native structure of SCs are better preserved in intact mitochondria, we reproduced such experiments but expressing AOX in the mitochondria of different cell models: (i) wild-type cells expressing AOX (CIV^{WT}AOX and E9AOX); (ii) cells lacking CIV which retain CI and SCI + III_2 superassembly due to the presence of AOX (CIV^{KO}AOX); (iii) cells that lack CIII which preserve CI due to AOX expression, note that in this case, CI cannot form SCs with CIII ($CIII^{KO}$AOX). AOX expressed in mammalian mitochondria is known to be functional and can recycle oxidized CoQ in cells lacking of mtDNA (*31*) or in cells lacking CIII or CIV (*12*). We described elsewhere that the expression of AOX prevents the degradation of CI in the absence of CIII or CIV (fig. S6A) (*12*). We found that the level of AOX activity was similar between the different cell lines (fig. S6B). To check whether the amount of AOX overexpressed was limiting for CI turnover, we performed flux control analysis of all cell lines. Titration with the CI inhibitor piericidin A clearly showed that AOX was not a limiting factor for CI, and in all cases, the obtained value was close to 1 (fig. S6, C to F, and table S3). Following similar reasoning to that reported in a recent work (*22*), the delivery of electrons from CI or CII to AOX should be independent of superassembly in the absence of CIII. However, if the superassembly between CI and CIII has any effect on the activity of CI, then in the absence of CIV, a change in the delivery of electrons from CI to AOX should be detected (Fig. 6A). In the two mutant cells, we detected measurable CI-AOX and CII-AOX respirations, while CIV-dependent respiration could not be recorded (Fig. 6B). Notably, while CII-AOX–dependent respiration was insensitive to the presence of CIII, CI-AOX–dependent respiration was significantly lower when CIII was present (Fig. 6B). This is true despite a higher NADH oxidation capacity of CI in CIV^{KO}AOX cells (Fig. 6C). We also reasoned that if a CoQ pool was shared between CII and CI, then addition of succinate would outcompete with glutamate + malate–based AOX respiration (Fig. 6D). We found that either in the wild-type or in the CIV^{KO} cells, all expressing AOX, the addition of succinate significantly increased the oxygen consumption over that achieved by CI substrates (fig. S7, A and B, and Fig. 6E). On the contrary, in $CIII^{KO}$ AOX cells, the addition of succinate was unable to increase the AOX-dependent oxygen consumption over that reached by CI substrates (fig. S7B and Fig. 6E). These results suggest that when CI is not superassembled, CoQ exists in a unique pool, whereas its superassembly triggers the formation of two partially differentiated pools.

We then measured directly NADH oxidation (Fig. 6F) in mitochondrial membranes from wild-type, CIV^{KO}, and $CIII^{KO}$ cell models, all expressing AOX, permeabilized by freezing and thawing. This analysis offered a number of interesting observations: (i) NADH oxidation of the two wild-type cell lines is different, being the E9 nuclear background significantly lower (≈50%) (Fig. 6F). We described elsewhere that this is due to the presence of a missense mutation in COI that reduce the activity of CIV and, hence, respiration (*32*), a fact that can also be observed in fig. S7 (A and B). (ii) The addition of succinate did not affect the oxidation of NADH in any wild-type cell line, while the inhibition of CIV by KCN almost completely abolished it in wild-type cells (Fig. 6F). (iii) The ablation of

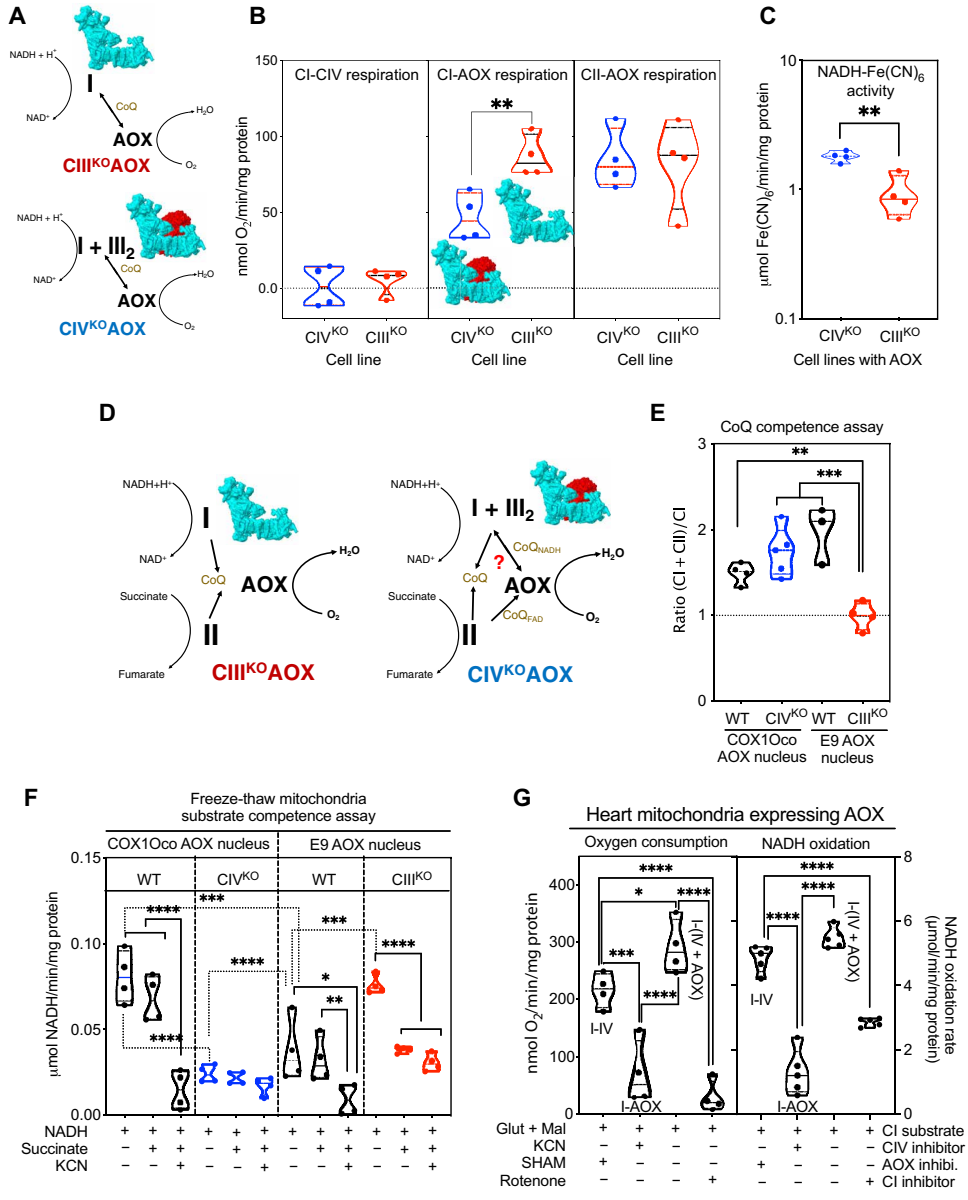

Fig. 6. The superassembly between CI and CIII modulates the activity of CI and functionally segments the CoQ pool. (**A**) Scheme representing the differential flux of electrons to AOX from the indicated mutant cell line. (**B**) Impact of the presence of CIII in the delivery of electrons from CI and CII to AOX. (**C**) Diphenyleneiodium (DPI)-sensitive NADH oxidation capacity of the mitochondrial preparation from the indicated cell line. (**D**) Scheme representing the simultaneous flux of electrons form either CI or CII to AOX from the indicated mutant cell line. (**E**) Estimation of the impact of the simultaneous addition of substrates for CII (succinate) on the CI-dependent respiration with CI substrates (glutamate and malate) in the presence or absence of CIII. (**F**) Impact of CIII and CIV superassembly on the maximum respiration capacity with CII (succinate) or CI (glutamate and malate) substrates versus both substrates added simultaneously. (**G**) Proportion of the maximum respiration achievable by CI substrates in the presence or absence of CI and CIII superassembly. (**H**) Analysis of the flux of electrons from NADH and CI or succinate and CII to AOX in the indicated freeze-thaw mitochondrial from wild-type (WT) cells or mutant cells lacking CIV or CIII all expressing AOX. (**I**) Flux of electrons from NADH and CI to AOX or CIV in intact heart mitochondria expressing AOX and monitored by oxygen consumption (left) or autofluorescence of NADH (right). *$P < 0.05$; **$P < 0.01$; ***$P < 0.001$; ****$P < 0.0001$.

CIV markedly reduced the rate of oxidation of NADH to levels equivalent to those caused by KCN (Fig. 6F). (iv) The ablation of CIII significantly increased the NADH oxidation with respect to the levels of their isogenic wild-type cells—which harbor a mutation in COI (Fig. 6F). This result parallels what we have observed measuring oxygen consumption in intact mitochondria (fig. S7, A and B) and fully confirms that the dependence of CIV activity limits the NADH oxidation capacity in E9-derived cells. (v) In the absence of CIII, but not of CIV, the addition of succinate significantly reduced the NADH oxidation, which, in these cells, is fully dependent on AOX (Fig. 6F). All these results demonstrate that the superassembly of CI with CIII, either in SCs or in the N-respirasomes, affects markedly in the NADH oxidation capacity of CI by modifying the delivery of electrons to CIV or AOX. Moreover, they indicate that CI and CII can potentially outcompete for delivering electrons to AOX, a phenomenon that is minimized by the presence of CIII.

To evaluate the impact of the mitochondrial source in the behavior of AOX, we generated a novel mouse model expressing AOX in

the heart and muscle mitochondria (see Materials and Methods for details) and repeated the experiments with purified wild-type muscle and heart mitochondria expressing AOX (fig. S7C). We first performed a flux control analysis, obtaining similar results to the cell lines, both with rotenone and piericidin A (fig. S7D and table S3). Next, we analyzed the respiration of intact mitochondria fed with CI substrates (Glut + Mal), assessing the distribution of electrons to either CIV or AOX by using specific inhibitors for each enzyme (Fig. 6G, left). As expected, more than 70% of CI-dependent respiration was sensitive to CIV inhibition, with a significant respiration mediated by AOX (Fig. 6G, left). We confirmed that this assay was specific for CI by monitoring NADH autofluorescence in intact mitochondria in the absence or presence of rotenone (Fig. 6G, right). We additionally performed experiments in freeze-thawed mitochondria prepared from hearts expressing AOX and confirmed again that NADH-linked respiration was completely inhibited by KCN, whereas CII-AOX respiration was maintained (fig. S7E). Monitoring NADH absorbance allowed us to confirm that KCN completely abolished NADH oxidation, in contrast to SHAM, which did not have any significant effect (fig. S7F). Similar results were obtained with mitochondrial preparations from muscle expressing AOX (fig. S7, G and H).

DISCUSSION

Overall, the more relevant conclusion of our work is that the formation of respiratory SCs modifies the kinetics and the flux of electrons occurring with nonsuper assembled complexes. In one side, the role of SCAF1 in the N-respirasome becomes now clear. After strong discrepancies, there is a general consensus that SCAF1 is required for the superassembly of the Q-respirasome (III_2 + IV) and to provide stability to the N-respirasome (*16*, *18*). There is also an agreement in that SCAF1 function is lost in the mutated form of SCAF1 that naturally arise in the C57BL/6 substrains (*5*, *17*). Despite that, BL6 heart mitochondria still assemble bona fide N-respirasomes, which are structurally different, less stable, and functionally impaired. These findings clarify the role of SCAF1 in the respirasomes and the relevance of the interaction between CIII and CIV. On the other side, the expression of AOX in cells and in mice and the ability to genetically control the free or superassembled status of CI allowed us to confirm that the delivery of electrons from CI but not CII to AOX or CIV is asymmetric only if the formation of SC I + III_2 is occurring.

Our results with AOX expression differ from previous interpretations (*22*). This discrepancy may be explained by methodological differences: (i) We measured both oxygen consumption and NADH oxidization, while the previous work only monitored NADH oxidation. (ii) We expressed AOX, a hydrophobic protein, in intact mitochondria both in cells and mice. In the previous report, AOX was expressed in and purified from *Escherichia coli* using DDM (a detergent that disrupt SC I + III_2 and SC I + III_2 + IV) and added to the assay medium containing submitochondrial particles. Although the AOX preparation was separated under a gravity flow to eliminate the excess of DDM, some detergent may remain attached to AOX, and its effect on the membranes after incubation at 32°C was not analyzed. (iii) We observed in our experiment that the NADH-dependent oxygen consumption and the NADH oxidation sensitive to CI inhibition were more efficient when performed throughout CIV than by AOX. On the contrary, in the previous work, NADH oxidation rate was higher by AOX than by the natural CIII and CIV contribution. This apparent discrepancy may be due to the presence in mitochondria of NADH dehydrogenases different from CI that may contribute to NADH oxidation (such as the apoptosis-inducing factor, which is not incorporated in SCs). These potential confounding effects were discarded in our assays by determining the rotenone/piericidin A NADH oxidation activity. However, in the previous work, this possibility was not evaluated. (iv) Last, the instability of SCs reported here may also contribute to the apparent discrepancy.

The present results confirm that superassembly of CI and CIII allows the retention of CoQ in a way that a partial segregation the CoQ pool allows substrate channeling, as classically defined (*33*). A very recent paper from Sazanov's group (*28*) studying the kinetic properties of NADH to Cyt c electron transfer by isolated SC I + III_2 also found that CoQ trapped within isolated respiratory SC I + III_2 limits CI turnover .

In addition to the major findings, we exhaustively reevaluated the mitochondrial BNGE profiles from a variety of murine sources and analyzed the stability of the sample under several conditions using advanced data-independent proteomics. This analysis provides relevant new knowledge to better interpret BNGE analysis. In one hand, the Blue-DiS technology allowed us to confirm from a true hypothesis-free perspective the presence, composition, and stoichiometry of the OXPHOS CI, CIII, CIV, and CV in free and superassembled forms in a variety of mitochondrial types. Thus, while the protein composition of these complexes is maintained, the proportion of OXPHOS SCs is tissue specific. Moreover, we demonstrate that regardless of the different positions where the respirasome migrate, it substantially maintains a constant stoichiometry of I + III_2 + IV, a result that is in full agreement with the different cryo–electron microscopy–derived structures published to date (*6*–*8*, *34*). This estimation stresses the necessity to correct the experimentally unsupported tendency to assume that the different bands of the respirasome contain increasing amounts of complex IV and to define the band with the faster migration rate as the I + III_2 + IV respirasome and those with a higher apparent molecular weight as successive megacomplexes (*18*). It is advisable to restrict the use of the term megacomplex to define the association between SCs (*35*). Nevertheless, it is remarkable that the N-respirasome migrate persistently in multiple bands, a phenomenon that requires further investigation of the potential partners or differential lipid composition. The Blue-DiS analysis also confirmed that SCAF1 is the only detectable assembly factor which is present in SC containing CIII and CIV. On the other hand, we describe unequivocally the existence of previously unidentified supercomplexes, SCs: I + IV that comigrate between the free CI and SC: I + III_2 and I + IV_2 that comigrate with SC: I + III_2 and the comigration of CI with CIV in the area of the respirasomes. CI and CIV associations could be predicted from the evidence obtained by cryo–electron microscopy that the interaction between CI and $CIII_2$ is independent from that between CI and CIV (*6*, *8*). SC I + VI_2 was, however, unexpected. This previously unidentified SC, as well as some of the already known associations, may represent true SCs or partially disassembled elements from larger complexes. In any case, their characterization in the BNGE is of major relevance because they can lead to inaccurate interpretations. This may be the case of the proposed previously unidentified fast migrating respirasome (I + III_2 + IV) that comigrate with I + III_2, despite the different molecular weight, solely based on the fact that the CI, CIII, and CIV comigrate in the same band (*36*). The comigration of I + III_2 with I + IV_2 is a more plausible explanation, since they have a very similar molecular weight. The comigration CI with CIV in the

area of the respirasomes, well above SC: I + III_2, does not contain IV dimers, and the added molecular weight of CI and CIV does not justify its apparent molecular weight. The fact that 2D-BNGE/DDM splits CI and CIV suggests as the more plausible explanation that this comigration imply the presence of a SC I + IV that interact with an unknown partner. This additional SC may again flaw our interpretation of the BNGE gels. Thus, when the gels are performed with a steep gradient or short run (as it is the case of the more used precasted native gels), the SCs I + III_2 + IV (the faster migrating band) and this particular SC: (I + IV)* may overlap [as a potential example, see (*18*)] leading to the wrong interpretation solely based on the position of CIV that this band corresponds to a respirasome.

A third important discovery reported here is that the N- and Q-respirasomes, and at less extent SC I + III_2, are unstable after disruption of the mitochondrial membranes even if preserved at 4°C. This previously unnoticed phenomenon raises concerns in the interpretation of experiments aimed to measure the proportion and function of SCs when mitochondrial membrane integrity is not preserved. More notably, the loss of N- and Q-respirasomes is paralleled by the specific proteolytic processing of SCAF1 by calpain-1 that causes the processed form of SCAF1 to migrate together with CIV. If this cleavage is physiologically relevant needs to be further investigated, then at this point, it explains discrepant results in the literature, which considered SCAF1 as a shorter protein that acts as a mere isoform of CIV (*37*). By the same token, it may explain the unexpected presence of variable amounts of SCAF1 associated with free CIV. Our observation is also coherent with the description of two respirasome structures by several groups (*6*, *8*) that differ in the connection between III_2 and IV that is either present (tight respirasome) or absent (loose respirasome). Our finding also explains the reported conversion of the tight respirasome into the loose one with time (*6*). Therefore, these observations largely clarify the investigation of the functional role of the respiratory SCs using BNGE.

In summary, in this report, we show that superassembly between respiratory complexes substantially enhances the respiratory capacity of the electron transport chain while minimizing ROS production. Superassembly establishes a segmented CoQ pool through the association between CI and CIII, while SCAF1 plays a critical role in the III_2 + IV interaction affecting the structure and kinetic properties of the respirasome. Hence, SCAF1 is a key factor in the regulation of the energy metabolism, optimizing efficiency under high energy demands.

MATERIALS AND METHODS

Experimental design

This work was designed to solve the apparent contradictory results regarding the role of SCAF1 in the structure, function, and physiological implications of superassembly of respiratory complexes. For that purpose, we generate isogenic mouse models expressing the functional SCAF1, a nonfunctional SCAF1, and knockout for the expression of SCAF1. The exercise capacity of the different mouse models was assessed. We purify the N-respirasomes from those sources and analyze their structure and function. Last, we generate cell and animal models expressing AOX to evaluate the delivery of electrons from CI to either superassembled CIII or nonsuperassembled CIV.

Mouse generation

This study used mouse and cellular models which were generated in our laboratory. (i) C57BL/6JOlaHsd mice with the functional version of SCAF1 were generated as previously described (*16*). C57BL/6JOlaHsd mice knock out for SCAF1 were generated by microinjection of ES cells knock out in the first alleles from European Mouse Mutant Cell Repository (EuMMCR) in C57BL/6JOlaHsd blastocysts. Further, the blastocysts were implanted in a pseudopregnant female C57BL/6JOlaHsd. (ii) AOX-expressing mice were generated by genOway by targeted insertion of the AOX complementary DNA (cDNA) within the Rosa26 locus via homologous recombination in embryonic stem cells originally derived from 129 strains of mouse and injected into C57BL/6J blastocysts and then reimplanted into OF1 pseudopregnant and allowed to develop to term. After removal of the neocassette flanked by flippase recognition target sites, the selected knock-in animals were then systematically backcrossed for more than 20 generations to C57BL/6JOlaHsd background. The expression of the transgene is dependent on the Cre recombinase–mediated excision of a *Lox*P-flanked transcriptional "STOP" cassette upstream of the AOX cDNA. For this study, we induce the expression of AOX in the muscle and heart by breeding the AOX animals with expressing CRE under the Actin Alpha 1 promoter.

Mouse experimentation

All animal procedures conformed to EU Directive 86/609/EEC and Recommendation 2007/526/EC regarding the protection of animals used for experimental and other scientific purposes, enforced in Spanish law under Real Decreto 1201/2005. Approval of the different experimental protocols requires the estimation of the adequate sample size as well as the definition of the randomization and blinding criteria. The mice were fed a standard chow diet (5K67, LabDiet).

Maximal incremental running test

Mice were forced to run on a treadmill at 20° slope [LE8700 (76-0303), Treadmill Panlab, Harvard Apparatus]. After a minute of acclimatization at 10 cm/s, the speed was increased up to 16 cm/s for 5 min and further every 2 min by 3 cm/s until exhaustion, which was considered reached when the mouse spent 3 s in the back of the rack.

Cellular models

All cell lines were grown in Dulbecco's modified Eagle's medium (Gibco BRL) supplemented with 5% fetal bovine serum (Gibco BRL). mtDNA-less mouse cells were generated by long-term growth of the L929 mouse cell line (ATCC CCL-1) in the presence of high concentrations of ethidium bromide as previously described (*32*). Control cells (control cells) were generated by transformation of ρ°929neo cells by cytoplast fusion using NIH3T3 fibroblasts as mitochondrial donors.

Blue native gel electrophoresis

SC levels and compositions were analyzed in isolated mitochondria from different tissues and cells by BNGE (*38*). Mitochondrial proteins from heart tissue were solubilized with 10% digitonin (4 g/g; Sigma-Aldrich D5628) and run on a 3 to 13% gradient Blue native gel. The gradient gel was prepared in 1.5-mm glass plates using a gradient former connected to a peristaltic pump. After electrophoresis, the gels were further processed for proteomic analysis, Western blotting, 2D SDS-PAGE, or 2D-BNGE (DDM) analysis. For 2D SDS-PAGE, the first-dimension lanes were excised from the gel, incubated for 1 hour at room temperature (RT) in 1% SDS and 1% β-mercaptoethanol, and run in a 16.5% denaturing gel. For 2D-BNGE (DDM) and 2D-BNGE digitonin, first-dimension lanes were excised from the gel and run in a 3 to 13% gradient gel in native condition adding 0.02% of DDM to the cathode buffer.

Immunodetection of complexes and SCs

After BNGE, 2D-BNGE/DIG, 2D-BNGE/DDM, or 2D-BNGE/PAGE, proteins were electroblotted onto polyvinylidene difluoride (PVDF) transfer membrane (Immobilon-FL, 0.45 μm; Merck Millipore, IPFL00010) for 1 hour at 100 V in transfer buffer (48 mM tris, 39 mM glycine, and 20% ethanol). A Mini Trans-Blot Cell system (Bio-Rad) was used. Sea Blocking buffer (Thermo Fisher Scientific 37527) or phosphate-buffered saline (PBS) with 5% bovine serum albumin (BSA) was used for 1 hour at RT to avoid nonspecific binding of antibodies. For protein detection, antibodies were incubated with the membrane for 2 hours at RT. Secondary antibodies were incubated for 45 min at RT. The membrane was washed three times with PBS 0.1 % Tween-20 for 5 min between primary and secondary antibodies, and after secondary antibodies, the last wash was only with PBS. To study SC assembly, the PVDF membrane was sequentially probed with antibodies complex I (anti-NDUFA9, Abcam ab14713), complex IV (anti-COI, Invitrogen 35-8100), complex III (anti-UQCR2, Proteintech), SCAF1 (anti-COX7A2L, St. John's laboratory STJ42268. This antibody was generated by immunization of rabbit with keyhole limpet hemocyanin–conjugated synthetic peptide between 37 and 65 amino acids from the central region of human COX7A2L. It recognizes an epitope in the common part of full-size and processed SCAF1, allowing to visualize the processed SCAF1 migrated with CIV after calpain processing as in Fig. 5 (C and F). This antibody was discontinued and substituted by the anti-COX7A2L (St. John's laboratory STJ110597), produced with a full-length recombinant human COX7A2L that, under the same experimental conditions, does not recognize the calpain-1–processed SCAF1 that needs to be identified only by MS.

Proteomics by DiS MS

DiS is a data-independent acquisition method that covers all possible fragmentations of precursors in the 400 to 1100 *m*/*z* (mass/charge ratio) range in two liquid chromatography–MS runs and has already been successfully used to study the mitochondrial proteome (*16*). DiS uses narrow tandem MS (MS/MS) windows of 2 *m*/*z*, typical of data-dependent acquisition methods, allowing direct peptide identification by database searching and FDR (false discovery rate) control by using a conventional target/decoy competition strategy, without requiring peptide fragmentation libraries. The Blue-DiS workflow generated a permanent, multidimensional, high-resolution, time-fragment mass map for all possible precursors present in each BNGE fraction and each mitochondrial sample, from which quantitative protein maps can be straightforwardly obtained with minimal computation. BNGE gels were excised in 26 slices taking as reference some discrete Coomassie-stained bands: slice 6 corresponds to a band that mainly contains SC I + III_2, slice 10 to CV, slice 12 to free $CIII_2$, and slice 15 to free CIV. All slices were cut into cubes (2 mm by 2 mm), reduced with 10 mM dithiothreitol (GE Healthcare), alkylated with 55 mM iodoacetamide (Sigma-Aldrich), and subjected to a standard overnight in-gel digestion at 37°C with 3 μg of sequencing grade trypsin (Promega, Madison, WI, USA) in 100 mM ammonium bicarbonate (pH 7.8). After desalting with C18 Omix cartridges (Agilent Technologies), the resulting tryptic peptide mixtures were injected onto a C-18 reversed-phase (RP) nano-column (75 μm inner diameter and 50 cm; Acclaim PepMap, Thermo Fisher Scientific, San José, CA, USA) using an EASY-nLC 1000 liquid chromatography system (Thermo Fisher Scientific, San José, CA, USA) and analyzed in a continuous gradient consisting of 8 to 31% B for 130 min and 50 to 90% B for 1 min (B = 0.5% formic acid in acetonitrile). Peptides were eluted from the RP nanocolumn at a flow rate of ~200 nl min^{-1} to an emitter nanospray needle for real-time ionization and peptide fragmentation in either a Q-Exactive or a Q-Exactive HF mass spectrometer (Thermo Fisher Scientific). Each sample was analyzed in two chromatographic runs covering different mass ranges (from 400 to 750 Da and 750 to 1100 Da, respectively). The DiS cycle consisted of 175 sequential High Collision Dissociation (HCD) MS/MS fragmentation events with 2-Da windows that covered the whole 350-Da range. HCD fragmentation was performed at a normalized collisional energy of 30, a resolution of 17,500, and a maximum injection time of 80 ms with the Automated Gain Control (AGC) set to a target of 3×10^5 ions. The whole cycle lasted 30 s or less depending on ion intensity during chromatography. Peptide identification was performed using Sequest running under Proteome Discoverer 1.4 (Thermo Fisher Scientific), allowing two missed cleavages, and using 2-Da and 20-ppm precursor and fragment mass tolerances, respectively. Met oxidation and Cys carbamydomethylation were selected as dynamic and static modifications, respectively. FDR for peptide identification was controlled using a separate inverted database and the refined method (*39*). Visualization, validation, and quantification of MS/MS spectra from specific peptides were performed using Vseq script, as described (*16*).

Protein and complex profiling

Quantitative protein migration profiles from Blue-DiS analyses were obtained by spectral counting, summing up the number of peptide-spectrum matches (PSMs) of all peptides identified for each protein on each slice of the gel. In the case of protein complexes, the total PSMs of the proteins contained in the complex were used for quantification. The normalized BNGE profile of each complex was constructed by calculating the slope from the plot of protein PSMs in a given slice versus protein PSMs in a slice used as reference (the one with the highest number of PSMs). The normalized abundance of each protein within a complex was calculated as the slope from the plot of PSMs of the protein in the different slices versus the PSMs of the most abundant protein from the complex in the same slices. The Gaussian deconvolution was performed in a hypothesis-free manner by a simultaneous least-squares fitting of the three normalized profiles adjusting the position, width, and height of each peak (thin lines) without any numeric constraint.

Determination of stoichiometry between complexes in SC

We observed that the number of PSMs for each protein, as calculated by DiS, was approximately proportional to the number of tryptic peptides detectable by MS (NOP) (fig. S3C, left). This finding agrees well with the use of the "protein abundance index" by other authors, which normalizes spectral counts by the number of detectable peptides (*40*). This consideration allowed us to calibrate the individual MS response of each protein, generating an estimation of the effective NOP (fig. S3C, right). By plotting, per each complex, the PSMs of the proteins against their effective NOP, we could estimate from the slopes the molar stoichiometries of complexes within each slice (fig. S3D).

Activity of complexes or N-respirasomes from BNGE-eluted bands

CD1, BL6:S^{111}, and BL6:S^{113} heart mitochondria were extracted, processed, and run in BN-PAGE as described above. CI, $CIII_2$, CIV monomer or respirasome bands were quickly excised from gels and

minced on ice. The grist was immediately resuspended in Medium MAITE sucrose 25 mM, sorbitol 75 mM, KCl 100 mM, EDTA 0.05 mM, MgCl2 5 mM, tris-HCl 10 mM (pH7.4), ortophosphoric acid 10 mM and respirasomes eluted by twirling for 4 hours at 4°C. Elution was collected and mixed with the appropriate volume of MAITE + BSA (2.5 mg/ml) at 37°C to reach 1 ml. Reaction was started by adding 100 μM NADH, 130 μM CoQ_1, 130 μM reduced decylubiquinone, 100 μM oxidized Cyt c. NADH, oxidized CoQ_1, and Cyt c levels were tracked by recording absorbance at 340, 289, and 550 nm, respectively, for 240 s in a UV-visible spectrophotometer. Optimal absorbance values were calculated by titration of each reactive in MAITE + BSA (2.5 mg/ml). DQ maximal absorbance peak could not be estimated due to the consequent turbidity of its dissolution in an aqueous environment. Baseline NADH oxidation and CoQ_1 reduction from the same elution were recorded after addition of 1 μM rotenone. Baseline Cyt c reduction from the same elution was recorded after addition of 2.5 μM antimycin A. Baseline Cyt c oxidation from the same elution was recorded after addition of 1 mM KCN.

Oxygen consumption by BNGE N-respirasome bands

CD1, BL6:S^{111}, and BL6:S^{113} heart mitochondria were extracted, processed, and run in BN-PAGE as described above. CIV monomer or respirasome bands were quickly excised from gels and minced on ice. The grist was immediately resuspended in MAITE + BSA (2.5 mg/ml) at 37°C and introduced in an Oxytherm System S1/MINI. Reaction was started by adding 100 μM reduced Cyt c for CIV monomer or 100 μM NADH for respirasomes. Oxygen levels were tracked for at least 180 s, and baseline oxygen consumption was recorded after addition of 1 mM KCN for CIV monomer or 1 μM rotenone for respirasomes.

H_2O_2 production by N-respirasomes from BNGE-eluted bands

CD1, BL6:S^{111}, and BL6:S^{113} heart mitochondria were extracted, processed, and run in BN-PAGE as described above. Respirasome bands were quickly excised from gels and minced on ice. The grist was immediately resuspended in Medium MAITE and respirasomes eluted by twirling for 4 hours at 4°C. Elution was collected and mixed with Amplex Red solution (Molecular Probes), following the manufacturer's instructions. Reaction was started by adding 100 μM NADH or 100 μM $CoQH_2$ + 1 μM rotenone. Amplex Red levels were tracked by recording fluorescence at 540/590 nm (excitation/emission) for 2400 s in a Fluoroskan Ascent fluorimeter (Thermo Labsystems). Baseline Amplex Red fluorescence from the same elution was recorded after addition of superoxide dismutase and catalase (5 U/ml).

NADH oxidation monitoring in intact mitochondria by autofluorescence

AOX-expressing heart mitochondria were extracted as described above and immediately resuspended in medium MAITE at 4°C. Mitochondria were mixed with the appropriate volume of MAITE + BSA (2.5 mg/ml) at 37°C to reach 100 μl. Reaction was started by adding 5 mM Glu + 5 mM Mal ± 1 mM KCN, 5 mM SHAM, or ± 1 μM rotenone. NADH levels were tracked by recording autofluorescence at excitation/emission of 340/475 nm for 20 min in a Fluoroskan Ascent fluorimeter (Thermo Labsystems).

Oxygen consumption measurement

AOX-expressing heart mitochondria of mitochondria from AOX-expressing cell lines were extracted as described above and immediately resuspended in medium MAITE at 4°C. To permeabilize mitochondrial membranes, mitochondria were subjected to a freeze-thaw step. Intact or freeze-thawed mitochondria were mixed with the appropriate volume of MAITE + BSA (2.5 mg/ml) at 37°C and placed in an Oxytherm System S1/MINI. Reaction was started by adding 5 mM Glu + 5 mM Mal ± 10 mM succinate ± 1 mM KCN, 5 mM SHAM, or ±1 μM rotenone. Permeabilized mitochondria were provided with 100 μM NADH or 100 μM CoQ_1H_2. Baseline levels were recorded after addition of 1 μM rotenone or 5 mM SHAM.

Activity of complexes in freeze-thaw mitochondria

AOX-expressing heart mitochondria of mitochondria from AOX-expressing cell lines were extracted as described above. Mitochondria were immediately resuspended in medium MAITE and subjected to a freeze-thaw step. Freeze-thaw mitochondria were mixed with the appropriate volume of MAITE + BSA (2.5 mg/ml) at 37°C to reach 1 ml. Reaction was started by adding 100 μM NADH, and in some cases, 1 mM $Fe(CN)_6$, 1 μM rotenone + 1 μM antimycin A, 100 μM succinate, or 1 mM KCN was added to the reaction mixture. Since the accessibility of CoQ analogs could be differential across the different AOX cell models (i.e., with or without SCs), we performed diphenyleneiodium (DPI)–sensitive NADH:$Fe(CN)_6$ activity (i.e., an activity for flavin mononucleotide in CI) which allowed us to quantify CI content. NADH and $Fe(CN)_6$ levels were tracked by recording absorbance at 340 and 412 nm, respectively, for 240 s in a UV/VISJASCO spectrophotometer. Baseline NADH consumption from the same sample was recorded after addition of 1 μM rotenone. Baseline $Fe(CN)_6$ absorbance from the same sample was recorded after addition of 5 μM DPI.

Statistical analysis

Unless specified, statistical analyses and graphics were produced with GraphPad Prism 8 software. Datasets were compared by *t* test, analysis of variance (ANOVA), or nonparametric analysis when corresponded and with *P* values adjusted for multiple tests. Differences were considered statistically significant at *P* values below 0.05. $*P < 0.05$; $**P < 0.01$; $***P < 0.001$; $****P < 0.0001$. All results are presented as means ± SD or means ± SEM.

SUPPLEMENTARY MATERIALS

Supplementary material for this article is available at http://advances.sciencemag.org/cgi/content/full/6/26/eaba7509/DC1

View/request a protocol for this paper from *Bio-protocol*.

REFERENCES AND NOTES

1. H. Schagger, K. Pfeiffer, Supercomplexes in the respiratory chains of yeast and mammalian mitochondria. *EMBO J.* **19**, 1777–1783 (2000).
2. H. Schägger, Respiratory chain supercomplexes of mitochondria and bacteria. *Biochim. Biophys. Acta Bioenerg.* **1555**, 154–159 (2002).
3. H. Eubel, L. Jänsch, H.-P. Braun, New insights into the respiratory chain of plant mitochondria. supercomplexes and a unique composition of complex II. *Plant Physiol.* **133**, 274–286 (2003).
4. R. Acín-Pérez, P. Fernández-Silva, M. L. M. L. M. L. Peleato, A. Pérez-Martos, J. A. Enriquez, Respiratory active mitochondrial supercomplexes. *Mol. Cell* **32**, 529–539 (2008).
5. E. Lapuente-Brun, R. Moreno-Loshuertos, R. Aciń-Pérez, A. Latorre-Pellicer, C. Colaś, E. Balsa, E. Perales-Clemente, P. M. P. M. Quirós, E. Calvo, M. A. Rodríguez-Hernández, P. Navas, R. Cruz, Á. Carracedo, C. Loṕez-Otín, A. Peŕez-Martos, P. Fernańdez-Silva, E. Fernańdez-Vizarra, J. A. Enríquez, Supercomplex assembly determines electron flux in the mitochondrial electron transport chain. *Science* **340**, 1567–1570 (2013).
6. J. A. Letts, K. Fiedorczuk, L. A. Sazanov, The architecture of respiratory supercomplexes. *Nature* **537**, 644–648 (2016).

7. J. Gu, M. Wu, R. Guo, K. Yan, J. Lei, N. Gao, M. Yang, The architecture of the mammalian respirasome. *Nature* **537**, 639–643 (2016).
8. J. S. Sousa, D. J. Mills, J. Vonck, W. Kühlbrandt, Functional asymmetry and electron flow in the bovine respirasome. *eLife* **5**, e21290 (2016).
9. D. Milenkovic, J. N. Blaza, N.-G. Larsson, J. Hirst, The enigma of the respiratory chain supercomplex. *Cell Metab.* **25**, 765–776 (2017).
10. E. Maranzana, G. Barbero, A. I. Falasca, G. Lenaz, M. L. Genova, Mitochondrial respiratory supercomplex association limits production of reactive oxygen species from complex I. *Antioxid. Redox Signal.* **19**, 1469–1480 (2013).
11. J. A. Enríquez, Supramolecular organization of respiratory complexes. *Annu. Rev. Physiol.* **78**, 533–561 (2016).
12. A. Guarás, E. Perales-Clemente, E. Calvo, R. Acín-Pérez, M. Loureiro-Lopez, C. Pujol, I. Martínez-Carrascoso, E. Nuñez, F. García-Marqués, M. A. Rodríguez-Hernández, A. Cortés, F. Diaz, A. Pérez-Martos, C. T. Moraes, P. Fernández-Silva, A. Trifunovic, P. Navas, J. Vazquez, J. A. Enríquez, The CoQH2/CoQ ratio serves as a sensor of respiratory chain efficiency. *Cell Rep.* **15**, 197–209 (2016).
13. J. Garaude, R. Acín-Pérez, S. Martínez-Cano, M. Enamorado, M. Ugolini, E. Nistal-Villán, S. Hervás-Stubbs, P. Pelegrín, L. E. Sander, J. A. Enríquez, D. Sancho, Mitochondrial respiratory–Chain adaptations in macrophages contribute to antibacterial host defense. *Nat. Immunol.* **17**, 1037–1045 (2016).
14. I. Lopez-Fabuel, J. Le Douce, A. Logan, A. M. James, G. Bonvento, M. P. Murphy, A. Almeida, J. P. Bolaños, Complex I assembly into supercomplexes determines differential mitochondrial ROS production in neurons and astrocytes. *Proc. Natl. Acad. Sci.* **113**, 13063–13068 (2016).
15. C. Greggio, P. Jha, S. S. Kulkarni, S. Lagarrigue, N. T. Broskey, M. Boutant, X. Wang, S. C. Alonso, E. Ofori, J. Auwerx, C. Cantó, F. Amati, Enhanced respiratory chain supercomplex formation in response to exercise in human skeletal muscle. *Cell Metab.* **25**, 301–311 (2017).
16. S. Cogliati, E. Calvo, M. Loureiro, A. M. Guaras, R. Nieto-Arellano, C. Garcia-Poyatos, I. Ezkurdia, N. Mercader, J. Vázquez, J. A. Enriquez, Mechanism of super-assembly of respiratory complexes III and IV. *Nature* **539**, 579–582 (2016).
17. J. A. Enríquez, Mind your mouse strain. *Nat. Metab.* **1**, 5–7 (2019).
18. T. Lobo-Jarne, E. Nývltová, R. Pérez-Pérez, A. Timón-Gómez, T. Molinié, A. Choi, A. Mourier, F. Fontanesi, C. Ugalde, A. Barrientos, Human COX7A2L regulates complex III biogenesis and promotes supercomplex organization remodeling without affecting mitochondrial bioenergetics. *Cell Rep.* **25**, 1786–1799.e4 (2018).
19. A. Mourier, S. Matic, B. Ruzzenente, N. G. Larsson, D. Milenkovic, The respiratory chain supercomplex organization is independent of COX7A2L isoforms. *Cell Metab.* **20**, 1069–1075 (2014).
20. R. Pérez-Pérez, T. Lobo-Jarne, D. Milenkovic, A. Mourier, A. Bratic, A. García-Bartolomé, E. Fernández-Vizarra, S. Cadenas, A. Delmiro, I. García-Consuegra, J. Arenas, M. A. Martín, N. G. Larsson, C. Ugalde, COX7A2L is a mitochondrial complex III binding protein that stabilizes the III2+IV supercomplex without affecting respirasome formation. *Cell Rep.* **16**, 2387–2398 (2016).
21. C. Bianchi, M. L. Genova, G. Parenti Castelli, G. Lenaz, The mitochondrial respiratory chain is partially organized in a supercomplex assembly. *J. Biol. Chem.* **279**, 36562–36569 (2004).
22. J. G. Fedor, J. Hirst, Mitochondrial supercomplexes do not enhance catalysis by quinone channeling. *Cell Metab.* **28**, 525–531.e4 (2018).
23. S. E. Calvo, K. R. Clauser, V. K. Mootha, MitoCarta2.0: An updated inventory of mammalian mitochondrial proteins. *Nucleic Acids Res.* **44**, D1251–D1257 (2016).
24. F. Diaz, H. Fukui, S. Garcia, C. T. Moraes, Cytochrome c oxidase is required for the assembly/stability of respiratory complex I in mouse fibroblasts. *Mol. Cell. Biol.* **26**, 4872–4881 (2006).
25. E. Perales-Clemente, E. Fernández-Vizarra, R. Acín-Pérez, N. Movilla, M. P. Bayona-Bafaluy, R. Moreno-Loshuertos, A. Pérez-Martos, P. Fernández-Silva, J. A. Enríquez, E. Fernández-Vizarra, R. Acín-Pérez, N. Movilla, M. P. Bayona-Bafaluy, R. Moreno-Loshuertos, A. Pérez-Martos, P. Fernández-Silva, Five entry points of the mitochondrially encoded subunits in mammalian complex I assembly. *Mol. Cell. Biol.* **30**, 3038–3047 (2010).
26. R. Moreno-Loshuertos, R. Acín-Pérez, P. Fernández-Silva, N. Movilla, A. Pérez-Martos, S. R. De Cordoba, M. E. Gallardo, J. A. Enríquez, Differences in reactive oxygen species production explain the phenotypes associated with common mouse mitochondrial DNA variants. *Nat. Genet.* **38**, 1261–1268 (2006).
27. H. Schägger, K. Pfeiffer, The Ratio of oxidative phosphorylation complexes I-V in bovine heart mitochondria and the composition of respiratory chain supercomplexes. *J. Biol. Chem.* **276**, 37861–37867 (2001).
28. J. A. Letts, K. Fiedorczuk, G. Degliesposti, M. Skehel, L. A. Sazanov, Structures of respiratory supercomplex I+III2 reveal functional and conformational crosstalk. *Mol. Cell* **75**, 1131–1146.e6 (2019).
29. J. R. Huertas, S. Al Fazazi, A. Hidalgo-Gutierrez, L. C. López, R. A. Casuso, Antioxidant effect of exercise: Exploring the role of the mitochondrial complex I superassembly. *Redox Biol.* **13**, 477–481 (2017).
30. J. N. Blaza, R. Serreli, A. J. Y. Jones, K. Mohammed, J. Hirst, Kinetic evidence against partitioning of the ubiquinone pool and the catalytic relevance of respiratory-chain supercomplexes. *Proc. Natl. Acad. Sci.* **111**, 15735–15740 (2014).
31. E. Perales-Clemente, M. P. P. Bayona-Bafaluy, A. Pérez-Martos, A. Barrientos, P. Fernández-Silva, J. A. Enriquez, A. Perez-Martos, A. Barrientos, P. Fernandez-Silva, J. A. Enriquez, Restoration of electron transport without proton pumping in mammalian mitochondria. *Proc. Natl. Acad. Sci. U.S.A.* **105**, 18735–18739 (2008).
32. R. Acin-Perez, M. P. Bayona-Bafaluy, M. Bueno, C. Machicado, P. Fernández-Silva, A. Pérez-Martos, J. Montoya, M. J. López-Pérez, J. Sancho, J. A. Enríquez, An intragenic suppressor in the cytochrome c oxidase I gene of mouse mitochondrial DNA. *Hum. Mol. Genet.* **12**, 329–339 (2003).
33. X. Huang, H. M. Holden, F. M. Raushel, Channeling of Substrates and Intermediates in Enzyme-Catalyzed Reactions. *Annu. Rev. Biochem.* **70**, 149–180 (2001).
34. M. Wu, J. Gu, R. Guo, Y. Huang, M. Yang, Structure of mammalian respiratory supercomplex I1III2IV1. *Cell* **167**, 1598–1609.e10 (2016).
35. R. Guo, S. Zong, M. Wu, J. Gu, M. Yang, Architecture of human mitochondrial respiratory megacomplex I2III2IV2. *Cell* **170**, 1247–1257.e12 (2017).
36. D. Sun, B. Li, R. Qiu, H. Fang, J. Lyu, Cell type-specific modulation of respiratory chain supercomplex organization. *Int. J. Mol. Sci.* **17**, 926 (2016).
37. K. Zhang, G. Wang, X. Zhang, P. P. Hüttemann, Y. Qiu, J. Liu, A. Mitchell, I. Lee, C. Zhang, J. Lee, P. Pecina, G. Wu, Z. Yang, M. Hüttemann, L. I. Grossman, COX7AR is a stress-inducible mitochondrial COX subunit that promotes breast cancer malignancy. *Sci. Rep.* **6**, 31742 (2016).
38. I. Wittig, H. P. Braun, H. Schägger, Blue native PAGE. *Nat. Protoc.* **1**, 418–428 (2006).
39. P. Navarro, J. Vázquez, a refined method to calculate false discovery rates for peptide identification using decoy databases. *J. Proteome Res.* **8**, 1792–1796 (2009).
40. Y. Ishihama, Proteomic LC–MS systems using nanoscale liquid chromatography with tandem mass spectrometry. *J. Chromatogr. A* **1067**, 73–83 (2005).

Acknowledgments: We are grateful to M. M. Muñoz-Hernandez, R. Martínez de Mena, and C. Jiménez for technical assistance. **Funding:** This study was supported by MINECO (SAF2015-65633-R), MCIU (RTI2018-099357-B-I00), CIBERFES (CB16/10/00282), and HFSP (RGP0016/2018) to J.A.E.; MINECO-BIO2015-67580-P and PGC2018-097019-B-I00, ISCIII-IPT13/0001 (ISCIII-SGEFI/FEDER, ProteoRed) the Fundació MaratóTV3 (grant 122/C/2015), and "la Caixa" Banking Foundation (project code HR17-00247) to J.V. The CNIC is supported by the Ministry of Economy, Industry and Competitiveness (MEIC) and the Pro-CNIC Foundation and is a Severo Ochoa Center of Excellence (MINECO award SEV-2015-0505). **Author contributions:** E.C., J.V., and J.A.E. conceived and designed the analysis. E.C. M.L.-L., F.G.-M., and J.C.S.-C. performed the proteomic analysis. S.C., A.G., P.H.-A., R.A.-P., Y.M.-M., and M.C.-A. performed the BNGE and the respirasomes functional analysis. S.C., M.C.-A., J.R.H., and R.A.C. performed the in vivo experiments. E.C., S.C., M.L.-L., J.V., P.H.-A., J.V., and J.A.E. interpreted the results. E.C., J.V., and J.A.E. wrote the paper. **Competing interests:** The authors declare that they have no competing interests. **Data and materials availability:** All data needed to evaluate the conclusions in the paper are present in the paper and/or the Supplementary Materials. Cell and mouse lines generated in this work can be requested to the corresponding author and will be delivered through and material transfer agreement. Additional data related to this paper may be requested from the authors.

Submitted 1 January 2020
Accepted 8 May 2020
Published 24 June 2020
10.1126/sciadv.aba7509

Citation: E. Calvo, S. Cogliati, P. Hernansanz-Agustín, M. Loureiro-López, A. Guarás, R. A. Casuso, F. García-Marqués, R. Acín-Pérez, Y. Martí-Mateos, J. Silla-Castro, M. Carro-Alvarellos, J. R. Huertas, J. Vázquez, J. A. Enríquez, Functional role of respiratory supercomplexes in mice: SCAF1 relevance and segmentation of the Q_{pool}. *Sci. Adv.* **6**, eaba7509 (2020).

Science Advances

Functional role of respiratory supercomplexes in mice: SCAF1 relevance and segmentation of the Q pool

Enrique Calvo, Sara Cogliati, Pablo Hernansanz-Agustín, Marta Loureiro-López, Adela Guarás, Rafael A. Casuso, Fernando García-Marqués, Rebeca Acín-Pérez, Yolanda Martí-Mateos, JC. Silla-Castro, Marta Carro-Alvarellos, Jesús R. Huertas, Jesús Vázquez and J. A. Enríquez

Sci Adv **6** (26), eaba7509.
DOI: 10.1126/sciadv.aba7509

Science Advances (ISSN 2375-2548) is published by the American Association for the Advancement of Science, 1200 New York Avenue NW, Washington, DC 20005. The title *Science Advances* is a registered trademark of AAAS.